Observed Synoptic-Scale Variability during the Developing Phase of an ISO over the Indian Ocean during MISMO

MASAKI KATSUMATA

Research Institute for Global Change, Japan Agency for Marine-Earth Science and Technology, Yokosuka, Japan, and Department of Atmospheric Science, Colorado State University, Fort Collins, Colorado

RICHARD H. JOHNSON AND PAUL E. CIESIELSKI

Department of Atmospheric Science, Colorado State University, Fort Collins, Colorado

(Manuscript received 4 November 2008, in final form 1 June 2009)

ABSTRACT

A case study of an intraseasonal oscillation (ISO) is investigated in the period leading up to its convectively active phase during the Mirai Indian Ocean Cruise for the Study of the MJO-Convection Onset (MISMO), which was conducted during boreal autumn 2006. Detailed observations, including apparent heat and moisture analyses, reveal that synoptic-scale variability of heat and moisture sources and sinks associated with the passage of three eastward-propagating cloud systems (EPCSs) was prominent during this period. These systems with periods of ~6 days propagated through the MISMO domain, priming the atmosphere for a convectively active phase of the ISO. The prominent shallow heating during this period may explain the rather slow (8 m s^{-1}) propagation speed for EPCSs. The zonal structure and sign of the frictional convergence show that these EPCSs have common characteristics to the frictional Kelvin mode studied by Ohuchi and Yamasaki. With the analyses of the period-averaged vertical profiles, the EPCSs were identified as the principal mechanism to moisten the atmosphere prior to the ISO convectively active phase.

1. Introduction

The Madden–Julian oscillation (MJO; Madden and Julian 1972) is the one of the most dominant modes of intraseasonal variability in the tropics. Although numerous studies have examined various aspects of the MJO (Zhang 2005), fundamental questions still remain as to the mechanisms for 1) initiating an MJO convectively active phase (hereafter "MJO active phase") in the Indian Ocean and 2) its slow propagation speed, especially in the eastern hemisphere (from the Indian Ocean to the western Pacific). Both questions have been discussed with the various hypotheses (e.g., Zhang 2005). On the other hand, key features of the MJO are its multiscale convective structure (e.g., Nakazawa 1988) and the essential role of moist convection (e.g., Hayashi and Sumi 1986). Although the internal structure of the MJO has been linked to convectively coupled equatorial waves (e.g., Masunaga et al. 2006) and to convective systems (e.g., Chen et al. 1996; Mori 1995), these relationships and interactions are still uncertain and require further study if we are to better understand the nature and characteristics of the MJO.

To understand the complicated internal structure of the MJO, a detailed dataset is needed to resolve its components (e.g., convective systems, tropical waves, and diabatic heating fields that link convection and waves). Generally such datasets are obtained primarily with special ground-based observations, although satellite observations and model reanalyses are becoming increasingly valuable in this regard as their quality and quantity continue to increase and improve. In the western Pacific, the Tropical Ocean Global Atmosphere Coupled Ocean–Atmosphere Response Experiment (TOGA COARE; Webster and Lukas 1992) was able to capture an MJO in its mature stage (Lin and Johnson 1996). However, until recently no ground-based dataset was available to study the onset stage of the MJO in the

Corresponding author address: Masaki Katsumata, Research Institute for Global Change, Japan Agency for Marine-Earth Science and Technology (JAMSTEC/RIGC), Natsushima-cho 2-15, Yokosuka 237-0061, Japan.
E-mail: katsu@jamstec.go.jp

DOI: 10.1175/2009JAS3003.1

Indian Ocean. In the autumn of 2006, the Mirai Indian Ocean Cruise for the Study of the MJO-Convection Onset (MISMO) project was carried out in the central Indian Ocean (Yoneyama et al. 2008b, hereafter Y08). The MISMO project successfully captured the onset of the convectively active phase of the intraseasonal oscillation (ISO).

Preliminary analyses from MISMO in Y08 suggest that convective systems with 5–7-day periods gradually moisten the middle and upper troposphere, and thus may play a role in preconditioning the atmosphere for deep convection. The preconditioning prior to the MJO active phase has been observed in previous studies (e.g., Kemball-Cook and Weare 2001), and the accumulation of the humidity is the process proposed in the MJO ''recharge–discharge'' theory of Bladé and Hartmann (1993). The roles and mechanisms of the convective systems in the preconditioning process have been discussed in previous studies (e.g., Lin and Johnson 1996; Johnson et al. 1999; Kikuchi and Takayabu 2004) in which the importance of shallow convection (cumulus and/or congestus) in moistening the free troposphere was noted. Although variability in time scales shorter than intraseasonal (e.g., synoptic-scale disturbances with time scales of a few to several days) has been reported in previous studies, this has not been their primary focus. For example, hypotheses on the MJO initialization over the Indian Ocean typically assume that the local forcing is ''stochastic'' (e.g., Yu and Neelin 1994). Recently, Maloney (2009), using a climate model, has shown that synoptic-scale variability in the western Pacific was suppressed before the convectively active phase of the intraseasonal oscillation. This study, as in previous ones, was focused on observations over the western Pacific, not over the Indian Ocean where MJO onset is typically observed.

The ultimate objective of the MISMO project is to reveal the mechanisms for onset of the MJO convectively active phase in the Indian Ocean. With this goal in mind, this study uses in situ observations over the Indian Ocean from MISMO to examine the synoptic-scale variability of the observed parameters, especially on the apparent heat and moisture fields in the period leading up to the ISO convectively active phase. In section 2, the MISMO analysis domain, observed datasets, and analysis methods used in this study are described. An overview of the convective activity during the observation period is presented in section 3. Then, temporal evolution of various fields over the MISMO domain is examined in section 4, with a focus on synoptic-scale variability. Possible mechanisms for these synoptic disturbances are investigated in section 5. In section 6, the synoptic-scale variability is related to ISO-scale variability. Summary and concluding remarks are given in section 7.

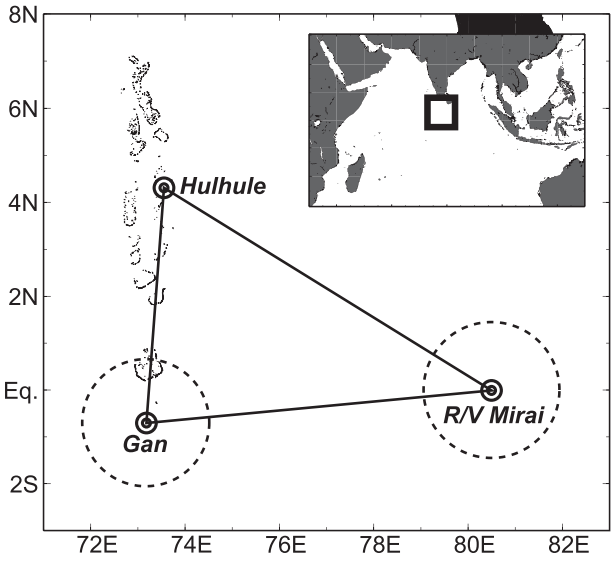

FIG. 1. Map of MISMO domain showing the observation sites used in this study. Inset map in upper right-hand corner shows the location of MISMO domain over the central Indian Ocean. The double circles indicate sounding observation sites. The broken circles indicate the maximum range of the radar coverage for volume scans.

2. Data and analysis method

Figure 1 shows the MISMO analysis domain (see Y08 for details). Within the MISMO observation period, three sounding sites—research vessel (R/V) *Mirai* at 0°, 80.5°E, Gan Island at 0.7°S, 73.2°E, and Hulhule Island at 4.2°N, 73.5°E—at the vertices of the MISMO triangle launched GPS Vaisala RS92 sondes from 31 October to 25 November [hereafter referred to as the arrayed sounding period (ASP)]. Within the ASP, the sonde launch frequency varied among these sites; every 3 h throughout the ASP at the R/V *Mirai*, every 12 h prior to 13 November and every 6 h thereafter at Gan, and every 12 h prior to 20 November and every 6 h thereafter at Hulhule. When necessary, sounding data were interpolated in time to facilitate a 6-h analysis frequency throughout the ASP at all sites. Soundings were corrected for a daytime dry bias as described in Yoneyama et al. (2008a).

In this study, sounding data are utilized to create time series plots at individual sites and averaged together to obtain a MISMO domain-mean. In addition, gridded fields of wind, temperature, and water vapor mixing ratio were created at 6 h, 1° horizontal, 25-hPa vertical resolution by objectively analyzing the sounding data using multiquadric interpolation (Nuss and Titley 1994).

These gridded fields were then used to diagnose divergence and vertical motion and to compute apparent heating (Q_1) and apparent drying (Q_2) following Yanai et al. (1973). In this study, area-averaged Q_1 and Q_2 are shown by averaging their gridded values within the MISMO triangle domain. This method of obtaining Q_1 and Q_2 is the same as in Johnson and Ciesielski (2000).

Along with the budget analyses, supplemental parameters are used. Latent (LE) and sensible heat (S) fluxes from the sea surface are obtained from the Woods Hole Oceanographic Institution (WHOI) objectively analyzed the air–sea fluxes (OAFlux) dataset, which is at 1° horizontal resolution (Yu et al. 2008). The dataset is averaged for the MISMO domain first, then it is adjusted by the ratio of the observed eddy fluxes at the R/V *Mirai* (Takahashi et al. 2005) to the OAFlux at the grid point closest to the R/V *Mirai*. The ASP mean adjustment ratio was 0.80 and 0.73 for latent and sensible heat flux, respectively. With this procedure, the OAFlux provides the temporal variation of the fluxes averaged over the MISMO domain, while their magnitude is adjusted to in situ observations from the R/V *Mirai*.

Tropical Rainfall Measuring Mission (TRMM) satellite-based estimates of radiative heating rate Q_R were obtained at 0.5° horizontal and 1-km vertical resolution from a product described in L'Ecuyer and Stephens (2003). The value is also used by averaging for the MISMO domain. A column-integrated Q_R can also be computed as a budget residual, $\langle Q_R \rangle = \langle Q_1 \rangle - \langle Q_2 \rangle - \mathrm{LE} - S$, where the angle brackets represent the vertical integral over the depth of the troposphere. In a fashion similar to the surface heat flux adjustment described above, the TRMM estimate of Q_R was adjusted to that of the budget-estimated Q_R. In this case, the ASP mean adjustment ratio was 0.86, and the ASP mean values of $\langle Q_R \rangle$ were -0.57 and -0.66 K day^{-1} for the budget residual and TRMM estimate, respectively. These estimates compare quite favorably to the TOGA COARE intensive flux array (IFA)–intensive observation period (IOP) mean $\langle Q_R \rangle$ value of -0.55 K day^{-1} (Ciesielski et al. 2003). Using these TRMM-adjusted estimates of Q_R, vertical divergence of the moist static energy (MSE) is derived as $Q_1 - Q_2 - Q_R = -\partial(\omega' h')/\partial p$, where $-\partial(\omega' h')/\partial p$ represents the vertical convergence of MSE due to unresolved vertical eddies as in Yanai et al. (1973).

Two radars, a C band on the R/V *Mirai* and an X band at Gan Island were operated to obtain volume scans every 10 min throughout the IOP. The reflectivity data are corrected as discussed in Katsumata et al. (2008a). To facilitate their use in various statistical analyses, the radar data are converted to a Cartesian coordinate with a resolution of 1 and 0.5 km in horizontal and vertical, respectively. Convective/stratiform flagging for each vertical column is determined by the method of Yuter et al. (2005) with classification parameters tuned accordingly for the radars used in MISMO.

Satellite-derived data are also used. Brightness temperature data from the infrared channel (IR-T_B) was obtained from *Meteosat-5*. These data covered the entire equatorial Indian Ocean during the MISMO IOP. Data from the Quick Scatterometer (QuikSCAT) satellite, produced by Remote Sensing Systems (http://www.remss.com), are used to derive surface wind analyses over the oceans.

3. Overview of convection during the arrayed sounding period

Whereas Y08 describes the temporal evolution of various fields during the MISMO IOP, the Hovmöller diagram of IR-T_B and the averaged IR-T_B over MISMO triangle, shown in Fig. 2, present an overview of convective activity during the ASP. Convection gradually increased over the MISMO domain through mid-November at which time convection became more intense and widespread. The lowest IR-T_B over the MISMO domain occurred around 19 November (18 November in 5-day running mean; 20 November in 1-day running mean). Convection after 16 November was identified as an MJO active phase by the method of Wheeler and Weickmann (2001) using filtered outgoing longwave radiation (OLR), as in Fig. 5 of Y08. Since the convection did not propagate across the Maritime Continent to the western Pacific, this event could be regarded as an aborted MJO. In this study, however, we will simply refer to this convective event as an ISO and investigate the period leading up to its active phase, focusing on the synoptic-scale variability and its contribution to the initialization process of the ISO-scale active convection.

4. Synoptic-scale variability prior to active period

a. Evidence from Y08

Using data primarily from the R/V *Mirai*, Y08 described significant variability on a 5–7-day time scale, which was suggested to play an important role in preconditioning the environment for deep convection. As shown in Y08, evidence for this synoptic-scale variability was found in 1) modulation of the SST diurnal cycle; 2) the number of congesti; 3) breaks in the mid- to upper-tropospheric divergence peak, the level of which continuously rose leading up to the convectively active period; and 4) the appearance of the widespread convective rain. On the other hand, the corresponding cloud activities are not determined in Y08 using OLR and wavenumber-frequency filter by the method of Wheeler and Weickmann (2001), as shown in Fig. 5 of Y08.

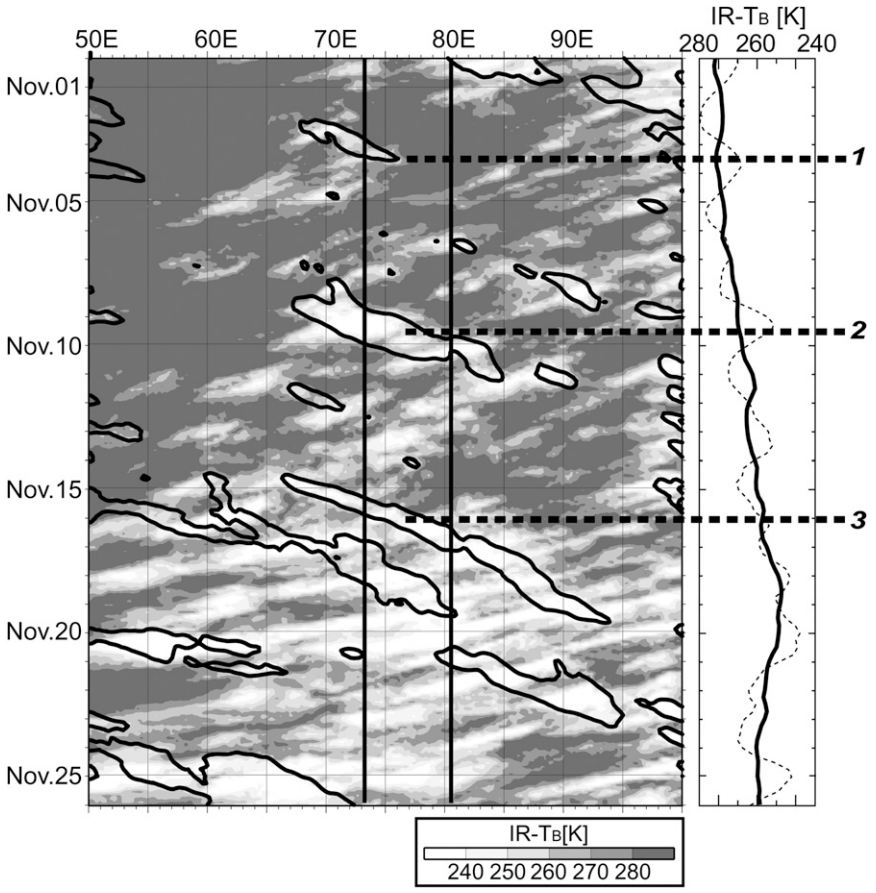

FIG. 2. (left) Hovmöller diagram of the IR-T_B averaged from 5°S to 5°N. The vertical solid lines indicate the longitudinal position of Gan Island (73.2°E) and R/V *Mirai* (80.5°E) for the analyses period. The contours are −10-K anomaly of eastward-propagating component (i.e., wavenumber >0) of the IR-T_B for all frequency range. (right) The IR-T_B averaged for over the MISMO triangle in Fig. 1. The solid and broken lines indicate the 5- and 1-day running means, respectively. The horizontal broken lines indicate the times when the EPCSs passed over the center of the MISMO triangle.

b. Clouds and precipitation

In the present study, the Hovmöller diagram of the hourly IR-T_B data from *Meteosat-5* (Fig. 2) can be used to help identify the disturbances that resulted in the synoptic-scale variability found in Y08. For example, there are many short-lived westward-propagating cloud packets that lasted only one day or so. Closer inspection reveals that the location of the appearance of these packets propagated eastward and passed over the MISMO domain. Y08 stated that widespread convective rain accompanied this eastward-propagating signal. These cloud systems are more readily seen when the strong negative anomaly (<10 K) of the eastward-propagating component is highlighted, as shown by the contours in Fig. 2. These eastward-propagating cloud systems (EPCSs) propagate with the speed of about 8 m s^{-1}. The speed and period (5–7 days) of the EPCS are slightly outside the range of the moist Kelvin wave used in the method of Wheeler and Weickmann (2001); thus, Fig. 5 of Y08 did not capture the EPCSs.

The EPCSs passed over the MISMO domain on 3, 9, and 16 November. Although Y08 did not mention the first one on 3 November (hereafter EPCS1), the contoured signal propagated eastward over Gan Island (73.2°E) but did not reach the R/V *Mirai* (80.5°E). The radar echo area around Gan Island (Fig. 3) indicates enhanced convective activity with all EPCSs, including EPCS1. This clearly shows that the EPCSs are more than just regions of enhanced cloudiness, but in fact contain precipitating convective clouds, even in EPCS1, which dissipated between Gan Island and R/V *Mirai*.

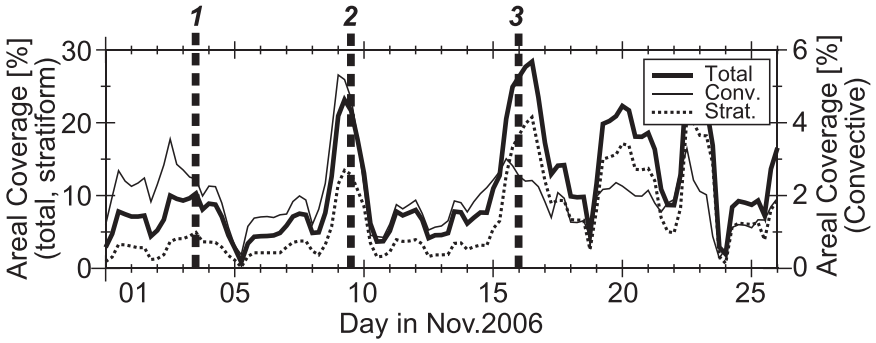

FIG. 3. Time series of the radar echo area for total, convective, and stratiform precipitation observed at Gan XDR, given as ratio of coverage to the observed horizontal area. The vertical broken lines are the same as in Fig. 2 to show the time when EPCSs passed.

c. *Moisture and heat variability*

The time–height plot of moist static energy (MSE) averaged over the MISMO domain is shown in Fig. 4b; here MSE $= c_pT + gz + L_vr$, where c_p is the specific heat of air, T is temperature, L_v is the latent heat of condensation, z is geopotential height, g is the gravitational constant, and r is the water vapor mixing ratio. The vertical growth of the high MSE layer leading up to the convectively active phase is readily seen. A close inspection of this plot shows that the vertical growth of the high MSE layer occurs in stepwise fashion. The days with significant vertical deepening of MSE are 3, 9, and 16 November, that is, coincident with EPCSs passing over the MISMO domain.

The effect of convection on the structure of MSE is shown by $-\partial(\omega' h')/\partial p$ in Fig. 5c. With the passage of each EPCSs, a couplet of $-\partial(\omega' h')/\partial p$ appears with large lower-tropospheric (below 4-km height) divergence and large middle- and upper-tropospheric convergence. This vertical couplet suggests a significant vertical transport of MSE from the lower troposphere to the middle and upper troposphere by convection associated with the EPCSs. Since variations in MSE are strongly tied to changes in the moisture field (see definition of MSE above), one interpretation of these results is that convection associated with the synoptic-scale disturbances, especially EPCSs, is responsible for the moistening of the middle and upper troposphere leading up to the convectively active phase. On the other hand, large values of Q_2, apparent drying, are observed with the passage of each EPCS. The precipitable water (Fig. 4a) also decreased after the passing of EPCSs. These observed facts are not contradicted because the MSE in the lower troposphere

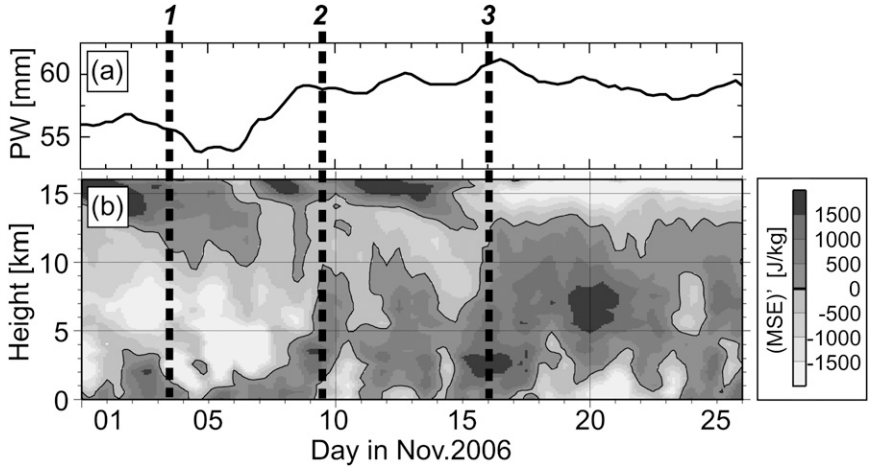

FIG. 4. (a) Time series of precipitable water and (b) time–height cross section of the moist static energy. Both are obtained by averaging three sounding sites. The value in (b) is displayed as the anomaly from the average for the ASP at each height. The vertical broken lines are the same as in Fig. 3.

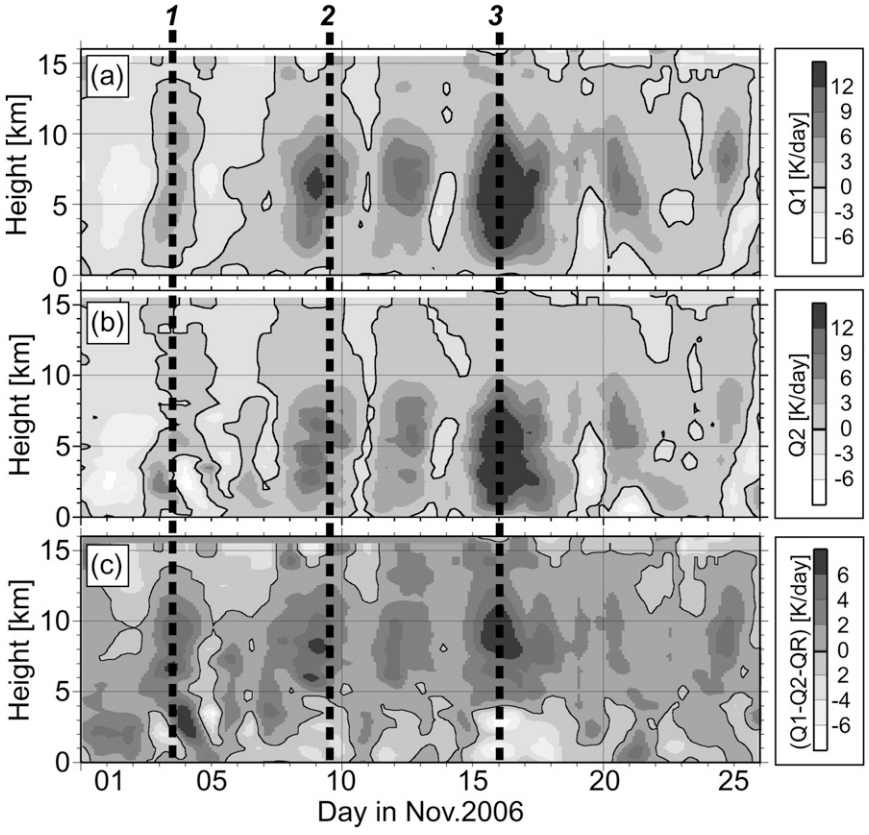

FIG. 5. Time height cross section of (a) Q_1, (b) Q_2, and (c) $-\partial(\omega' h')/\partial p$. The vertical broken lines are the same as in Fig. 3.

decreased after the passing of the EPCSs, as seen in Fig. 4b. These indicate that the EPCSs work to transport the water vapor from the lower troposphere to the middle and upper troposphere to extend the moist layer, while the total amount of the water vapor decreases as precipitation.

Finally, we note that the synoptic-scale variation of Q_1, Q_2, and $-\partial(\omega' h')/\partial p$ (Fig. 5) is more significant in the first half of the ASP than the second half, though convection was more intense and widespread in the second half, as shown in Fig. 2. Temporal variations of precipitation computed as a Q_2 budget residual compare well to estimates from rain gauges and satellites prior to the convectively active period, but show less agreement thereafter (Katsumata et al. 2008b). This suggests that the disturbances prior to the convectively active phase were well captured by the MISMO sounding array, but poorly resolved by the sounding network during the active phase.

5. Possible mechanisms for synoptic-scale variability

a. Propagation speed and ambient winds

Figure 2 indicates that the EPCS propagated eastward with the speed of about 8 m s^{-1}. This speed is comparable to that of typical environmental winds in the tropics, or gust front/gravity currents that are typical propagation mechanisms for convective systems. To examine whether the EPCSs motion was determined by advective effects, Fig. 6 shows the zonal wind profile averaged over the MISMO triangle using data from the three sounding sites. This plot clearly shows that the deep-layer wind was easterly (*westward*) in both the mean (Fig. 6b) and during the passage of the EPCSs (Fig. 6a). Therefore, advection cannot explain the motion of the EPCSs, which is *eastward* at ~8 m s^{-1}. Furthermore, given the easterly flow impeding the eastward progression of the relatively weak cold pools in this region, it is unlikely that gravity current dynamics can account for the eastward speed of motion. Thus, it is concluded that nonadvective effects—that is, wave dynamics—should be considered as a plausible propagation mechanism for these signals.

b. Vertical structure and periodicity

With a propagation speed of 8 m s^{-1} and a 6-day period, the characteristics of the EPCSs are slightly outside the normal range of the generally observed characteristics of the Kelvin wave described in Wheeler

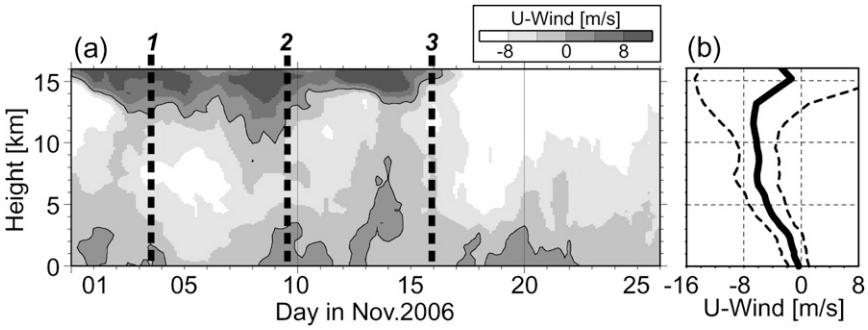

FIG. 6. Zonal wind averaged from three sounding points in MISMO triangle, in the form of (a) time–height cross section and (b) temporal average for entire period (solid) with a standard deviation (dotted). The height scale for both plots is to the left of (a). Vertical broken lines in (a) are the same as in Fig. 3.

and Kiladis (1999). On the other hand, if one considers all convective events in the preactive period (EPCS and intermediate convection; see Figs. 2 and 5), then the period could be regarded as 3 days, which accurately describes a Kelvin wave with the equivalent depth of about 25 m [which appears frequently in OLR as in Wheeler and Kiladis (1999)]. To investigate whether Kelvin wave dynamics can be applied to the present case, the vertical structure of the atmosphere is examined. To isolate EPCSs with 3–6-day periods, the radiosonde data are bandpass filtered to extract 1–8-day variability. Figure 7 shows this analysis using Gan Island data, since the EPCS signal is somewhat degraded at the R/V *Mirai* as described in the previous section.

Comparing the time–height cross sections to that of the composite analyses of a moist Kelvin wave in the eastern Pacific by Straub and Kiladis (2003b), we can find some similarities, especially in moisture and temperature anomalies. As discussed in the previous section, the moist region extends upward during the passage of the EPCS. The temperature anomaly shows a characteristic ''boomerang''-like structure with a warm anomaly below about 5 km and above 13 km prior to EPCS passage, with warm anomalies between 5 and 13 km during passage. Although the overall vertical structure of the zonal wind is unclear, the phase relationship between the temperature and zonal wind anomalies around the tropopause (Fig. 7c for time–height cross section, or Fig. 7d for time series at 16-km height) indicates that the westerly peak occurs between the positive and negative peaks of the temperature anomaly. This quadrature relationship agrees well with the theoretical structure of a linear equatorial Kelvin wave that propagates vertically.

We note that in this filtered view, the 6-day variation dominates, while the 3-day variation is difficult to see. Considering that the 6-day variation is more prominent in the OLR Hovmöller diagram (Fig. 2), in the heat and moisture budgets (Fig. 5), and the quadrature relationship between temperature and wind at the tropopause, the significant convection in the 6-day cycle is the primary mechanism to create the wave response, even though the 3-day cycle matches better to the frequently observed moist Kelvin wave (e.g., Takayabu 1994; Wheeler and Kiladis 1999). This suggests that the primary equivalent depth in the present case is shallower than that of the frequently observed moist Kelvin wave. In other words, shallower displacement might be important to make the 6-day cycle more significant than the 3-day cycle.

c. *Heating profile*

As described in the previous subsection, the EPCS characteristics do not match those of Kelvin waves reported in previous observationally based studies. The theoretical study by Ohuchi and Yamasaki (1997), however, showed that including the effects of surface friction in the moist Kelvin wave produces a slower propagation speed (less than 10 m s^{-1}), with slightly preceding moderate heating in the lower troposphere.

Gravity wave dynamics are another possibility for the propagation mechanism of the EPCSs. Various studies have shown that simplified convective- and stratiform-type vertical heating profiles are a source of gravity waves with much faster speeds than that of the EPCSs (e.g., Nicholls et al. 1991; Mapes and Houze 1995). On the other hand, recent numerical simulations by Tulich et al. (2007) and Tulich and Mapes (2008) found the existence of the very slow gravity waves with speeds of 11–12 and 7–8 m s^{-1} (''ultraslow'' and ''gust front wave'' in their papers, respectively) that were emitted from shallow, or high vertical wavenumber, heating sources. These later studies are examples of including ''shallow heating'' effects.

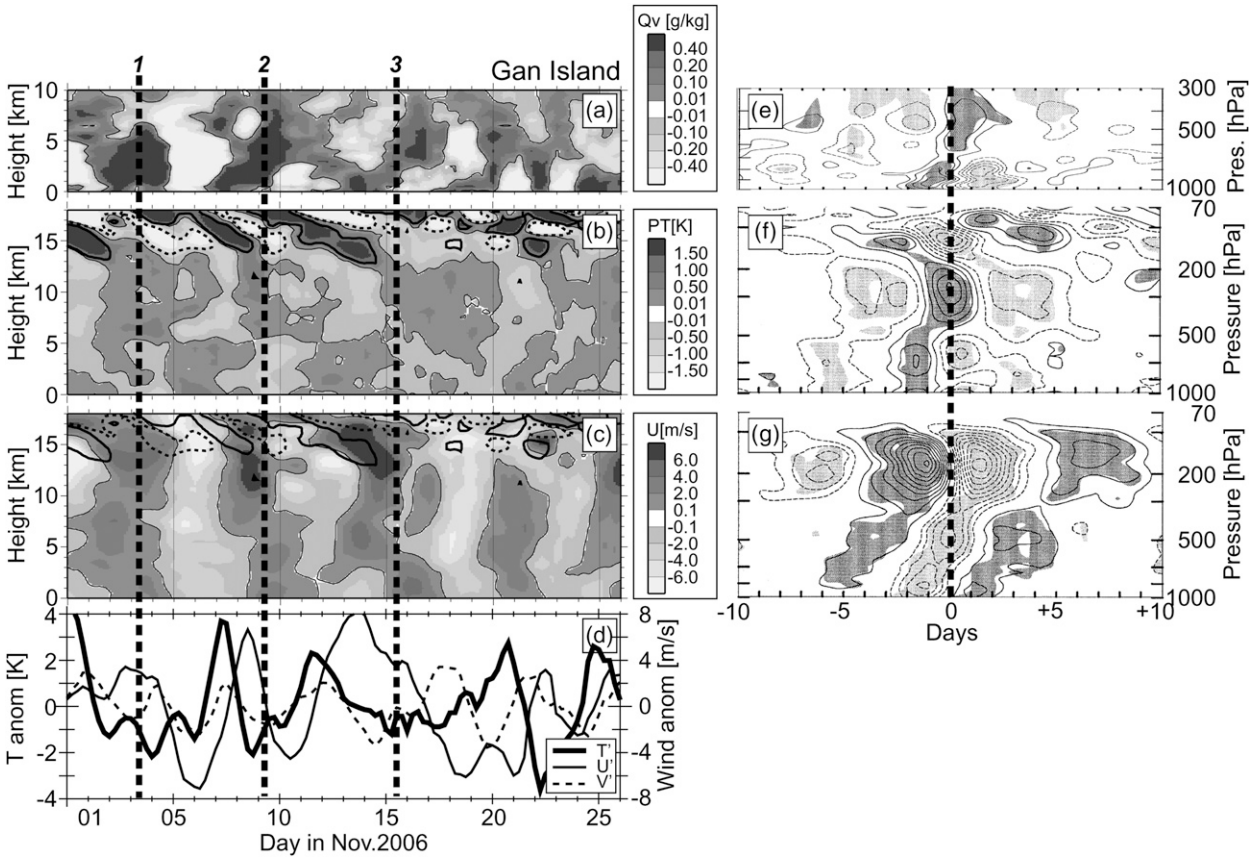

FIG. 7. Temporal variation of the radiosonde-observed fields at Gan Island, with the 1–8-day bandbass filter. The time–height cross sections are shown for (a) water vapor mixing ratio, (b) temperature, and (c) zonal wind. The values at 16-km height are plotted as the line graph in (d). (e)–(g) Same values as in (a)–(c), but quoted from Fig. 5 of Straub and Kiladis (2003b). The vertical broken lines in (a)–(d) are the same as in Fig. 3.

We now consider if shallow heating existed in the EPCSs, recognizing that these convective events included significant stratiform precipitation that typically results in top-heavy heating profiles. An inspection of the time–height cross section of the heating profile in Fig. 5 reveals that EPCSs include positive Q_1 throughout the layer below 10-km height to form an ''upright'' heating pattern with comparable heating rates both below and above 5-km height. On other days with large positive Q_1 (e.g., 12–13 and 20–21 November), the heating profile is ''top heavy'' with higher heating rates above the 5-km height than below.

To quantify these characteristics on the vertical heating profile, we calculate a simple index that indicates the structure of the heating profile. The heating profile index (HPI) is defined as

$$\mathrm{HPI} = [Q_1(\mathrm{UT}) - Q_1(\mathrm{LT})]/\mathrm{RR}_{\mathrm{SFC}},$$

where Q_1(UT) and Q_1(LT) are the averaged Q_1 between 600–300 and 900–600-hPa, respectively, and $\mathrm{RR}_{\mathrm{SFC}}$ is the surface rain rate calculated from the budget analyses. A large positive value of HPI implies a top-heavy profile, while small (or negative) implies a bottom-heavy profile. Some rough estimates of HPI for the previous studies are ~0.4 for TOGA COARE (Johnson and Ciesielski 2000) and ~0.15 for Marshall Island (Yanai et al. 1973). The total average for the MISMO ASP is 0.05. The temporal variation of the HPI in the present case (excluding rain rates less than 5 mm day^{-1}) is shown in Fig. 8. Focusing on the period of EPCSs (shaded), all EPCSs showed near-zero or negative HPI (i.e., relatively bottom-heavy heating) in their early stages. This suggests that the bottom-heavy heating was located in the eastern or leading edge of the EPCSs. In addition, an HPI value is ~0.1 throughout EPCS3. This implies that shallow heating was present in EPCS3, not only in its leading edge, but throughout this convective event.

Shallow heating is consistent with the proposed wave mechanism by Ohuchi and Yamasaki (1997) and Tulich and Mapes (2008); especially, their location in the leading edge of the convective packet matches to Ohuchi and

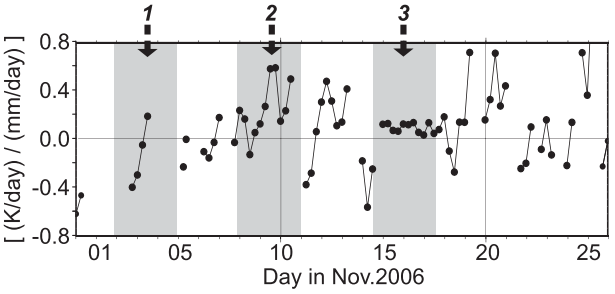

FIG. 8. The temporal variation of the value HPI. The shaded period is 3 days centered at the time when EPCS passed, as the vertical broken lines in Fig. 3. The HPI values are plotted only for the days with the surface rainfall larger than 5 mm day^{-1}.

Yamasaki (1997). In addition, we note that the abundance of the shallow- and stratiform-type convection and heating is also compatible with the ''shallow-CISK'' (conditional instability of the second kind) mechanism (Wu 2003), which could provide the moisture needed to sustain convection in the EPCS packet.

The corresponding convection can be seen in radar data. The frequency distribution of echo-top height at Gan XDR (Fig. 9) indicates that, during EPCS events, echo tops were more common below 5 km than on other days. The high frequency *below* 5 km could be regarded as a large population of shallow convective clouds (e.g., cumulus and congestus) (Johnson et al. 1999), whereas the peak *at* 5 km could be also caused by reasons other than congestus (e.g., bright band and melting effects).

An example of the shallow, eastward-propagating convection at the leading edge of the EPCSs is shown in Fig. 10 for the EPCS1. While each precipitating line developed and dissipated without significant movement, the new lines developed to the east of the previous ones. For the other EPCSs, eastward-moving radar echo lines could be identified with speeds less than that of EPCSs, while the altering of the line is unclear. These radar echo images suggest that 1) the shallow convection existed especially in the leading edge of the EPCSs, and 2) the EPCS and/or leading shallow convection propagate with the wave dynamics, not by advection.

Shallow heating was also present in the convective packets in between the EPCSs, although the shallow heating source or absolute amount of the heating was smaller than in the EPCSs. If the convection in between the EPCSs was also associated with an eastward-propagating signal, the driving mechanism could be same as the EPCSs.

d. Frictional convergence

Frictional convergence has been shown as a mechanism to foster moist Kelvin waves. (e.g., Wang and Rui 1990). In particular, the theoretical work by Ohuchi and Yamasaki (1997) found that slow ($<$10 m s^{-1}) moist Kelvin waves could result from frictional convergence. To examine this mechanism, Fig. 11d shows the time series of the surface divergence decomposed into its zonal ($\partial u/\partial x$) and meridional ($\partial v/\partial y$) components on and around the MISMO domain. Preceding each EPCS, surface convergence increases, dominated by changes in the meridional component. This suggests that frictional convergence ahead of each EPCS leads to a favorable thermodynamic environment for the EPCS. This relationship between increasing meridional convergence and decreasing convective inhibition (CIN) is observed even in the convectively active period (i.e., after mid-November).

The relationship between CIN and the convective parameters LCL and LFC can be seen by examining Figs. 11b and 11c. This comparison shows that changes in CIN are better correlated to those in the LFC than the LCL. This would indicate that the cooling (warming) of the environmental profiles contribute more to decreased (increased) CIN than the moistening and heating (drying

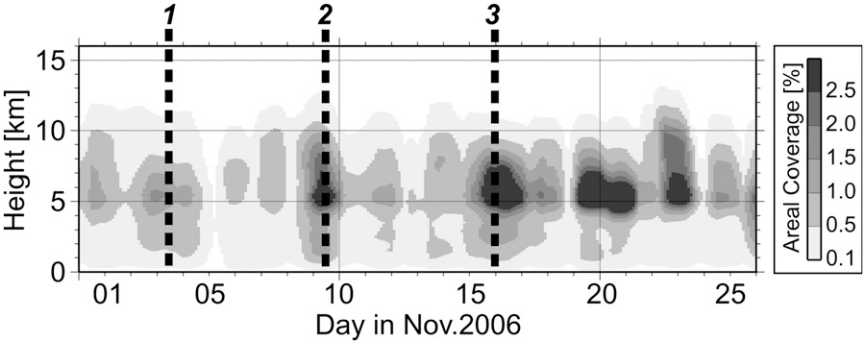

FIG. 9. Time–height cross sections of the area of the 10-dBZ echo-top height observed at Gan XDR, expressed as ratio of coverage to the observed horizontal area. The vertical broken lines are the same as in Fig. 3.

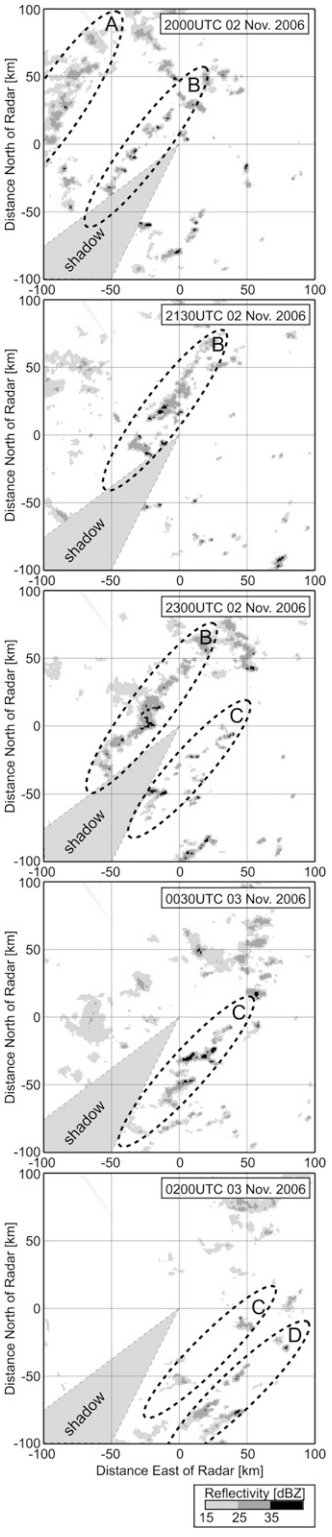

FIG. 10. Plan position indicator images of the Gan XDR at the elevation of 1.8°, at every 90 min from 2200 UTC 2 Nov to 0200 UTC 3 Nov. The broken envelopes labeled ''A'' to ''D'' indicate the lined radar echoes. The shaded area to the southwest indicates unobservable ''shadow'' area.

and cooling) of the lifted parcel (i.e., the air in the lower boundary layer). This further suggests that frictional convergence in the present case is more effective in the process of lifting the environmental air to decrease its temperature than the moistening and/or heating of the boundary layer.

e. Discussion

The above results indicate that the EPCSs 1) propagate and are not due to advective processes; 2) resemble the structure of vertically propagating Kelvin waves; 3) have shallow heating and convection, especially in the leading part of the convection packet; and 4) have frictional convergence ahead of the convection packet. These characteristics correspond to those of the frictional Kelvin mode in Ohuchi and Yamasaki (1997). Although their study relates the frictional Kelvin mode to the super cloud cluster (SCC) within the convectively active phase of the MJO, the resemblance of their study to the present case implies that this mode is important also in the period leading up to the convectively active phase. The appearance of the moist Kelvin wave prior to the ISO convectively active phase was similar to that in Straub and Kiladis (2003a), while the propagation speed differs from theirs. On the other hand, the gravity wave response to shallow heating, as in Tulich and Mapes (2008), could be also the driving mechanism of the EPCSs if we regard the deep convection and Kelvin wave structure in the EPCSs as a response to the shallow convection.

The convective signals in between the EPCSs are weaker but are also an important source of synoptic-scale variability. Like the EPCS, these signals contain shallow convection and propagate eastward at a similar speed. If both these signals are considered as a single wave type, a 3-day cycle with 8 m s^{-1} propagation speed corresponds well to a Kelvin wave observed ubiquitously over the globe (e.g., 17-m equivalent depth in Takayabu 1994; 25 m in Wheeler and Kiladis 1999). However, only the EPCSs with the 6-day cycle have the clear signal of the shallow convection, Kelvin wave-type atmospheric response, and frictional convergence. This also implies that the convective signal in between the EPCSs is caused by the different mechanism from the EPCSs. One possibility is the relationship of these convective signals to westward-propagating disturbances. Figure 12 shows that both the signals on 6 and 12 November appeared when the Northern Hemisphere side (5°–10°N) is cloudy, with southerly surface winds, and convergent to the north of the MISMO domain. The asymmetry of the convergence along equator, meridional wind, and their periodicity agrees well with that of the mixed Rossby–gravity wave, while the propagation speed is quite slow compared to that found in previous

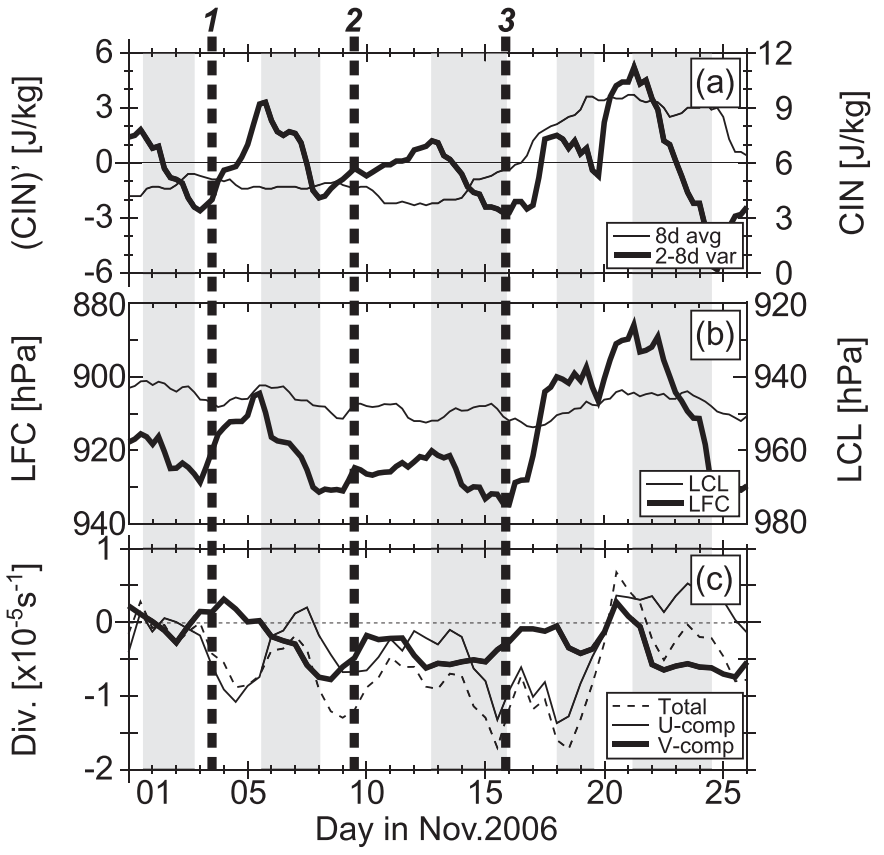

FIG. 11. Temporal variation of the (a) CIN, (b) LCL (thin) and LFC (thick), and (c) QuikSCAT-observed total and decomposed surface divergence. The values in (a) and (b) are averaged for three soundings in the MISMO array. The thin line in (a) is with 8-day running mean, while the thick line is with 2–8-day bandpass filter; (b) is applied 2-day running mean; (c) is averaged for 10° × 10° box centered at 0°, 75°E and 2-day running mean. The period of decreasing CIN is shaded.

studies (e.g., Hendon and Liebmann 1991). Further study is needed to clarify the mechanism for the convective signals that appear between the EPCSs.

6. ISO-scale variability

As discussed in Y08, some controversy exists as to whether the observed convectively active phase in the MISMO IOP is in fact an MJO. On the other hand, the synoptic-scale variance is enhanced leading up to the convectively active phase. To examine the evolution of the observed variance on the ISO time scale, the temporal evolutions of the observed parameters are displayed with a 5-day running mean, which has typically been used in previous studies to examine intraseasonal variation. Here we discuss the temporal variations in days relative to the minimum IR-T_B (19 November), similar to previous MJO studies that identify the convective peak with minimum OLR (e.g., Kiladis et al. 2005).

In the MISMO ASP, the moisture anomaly (Fig. 13a) becomes positive above the boundary layer after day −10. It gradually deepens to the upper troposphere toward day 0, with a large positive anomaly around 3-km height. Around day 0, the positive moisture anomaly reaches its peak around 6 km with a weak dry anomaly in the lower troposphere. This temporal evolution is quite similar to that observed in previous MJO studies (e.g., Kemball-Cook and Weare 2001).

A similar pattern is seen also in the Q_1 time series (Fig. 11b). The heating becomes positive about day −15 at about 2-km height. The maximum heating around 6–7 km appears around day −10. The maximum heating appears from day −5 to day 0 and weakens thereafter with a slight cooling in the lower troposphere. This time scale and temporal evolution of heating are consistent with those found in the previous MJO studies (e.g., Lin et al. 2004; Kiladis et al. 2005). These results indicate that the present

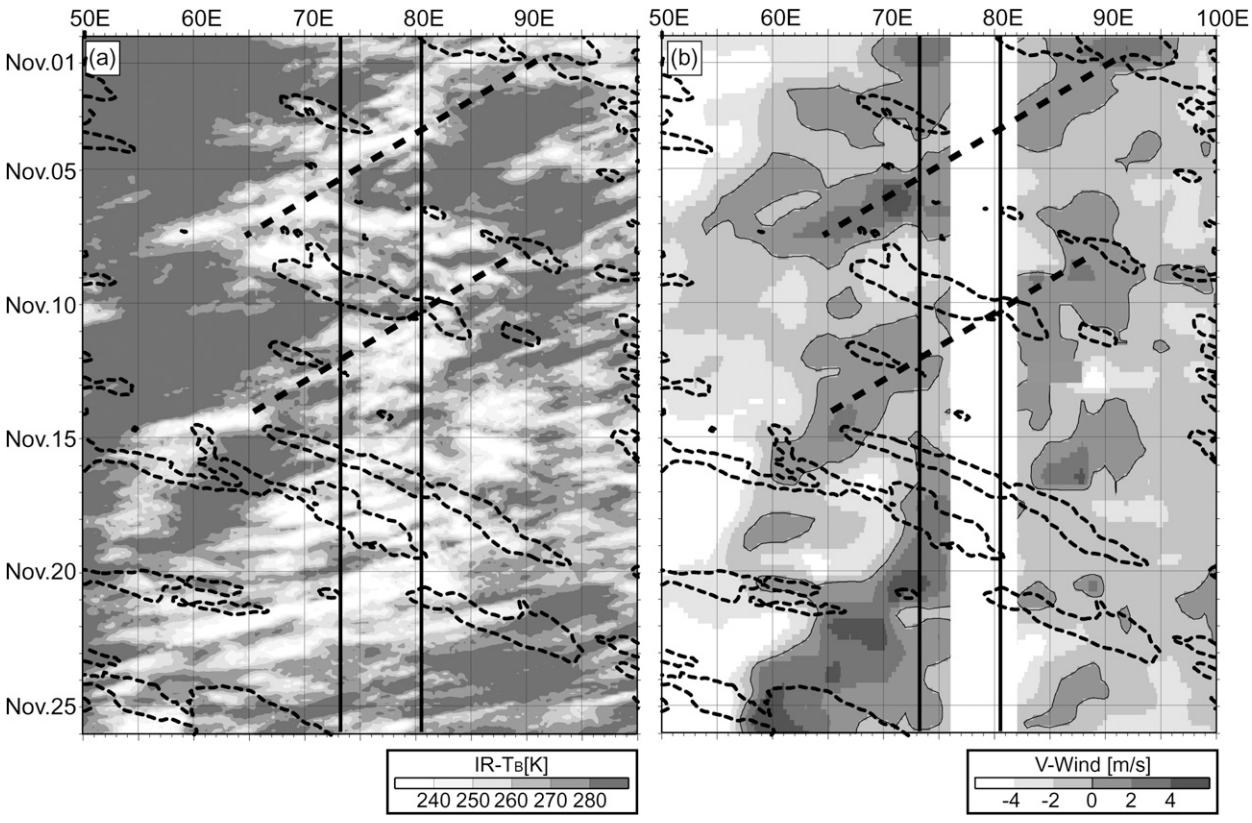

FIG. 12. Hovmöller diagrams created using data from 5° to 10°N. (a) IR-T_B. (b) QuikSCAT meridional wind. The vertical solid lines and contours are same as in Fig. 2. The thick broken lines connect westward-propagating minimum value of QuikSCAT meridional wind in (b) before 16 Nov. The area between 76° and 82°E is masked out in (b) because QuikSCAT winds are not available over land areas, in this case Sri Lanka and the southern tip of India.

case resembles previous analyses of MJOs in terms of structure and temporal evolution in the time scale of the ISO.

By comparing the ISO-scale variations (Fig. 13) and synoptic-scale variations (Figs. 4 and 5), the dates of the EPCSs corresponds to the characteristic dates in the ISO-scale variations. Near the time of EPCS1 on day −16, ISO-scale Q_1 turned positive. When EPCS2 passed on day −10, the ISO-scale moist layer extended vertically to 9 km, and the peak height in the moisture anomaly at 3 km and in the Q_1 at 6 km became apparent. Around the time of EPCS3 on day −3, maximum Q_1 at about 6-km height appeared, and the moist layer extends above 10-km height and negative moisture anomaly appeared below 2-km height. These correspondences suggest that the characteristic ISO-scale variability was a projection of the synoptic-scale variabilities.

In addition, the widespread cloudiness of the convectively active phase (Fig. 2) appeared just after the passing of EPCS3, implying that this convective event may have acted as a direct trigger for the cloud systems in the convectively active phase.

These results suggest that the synoptic-scale variation is an important contributor to the ISO-scale variation.

7. Summary and discussion

In boreal autumn 2006, the MISMO experiment was conducted in the central Indian Ocean. Using the unique dataset collected in MISMO, in particular radiosonde-based apparent heat and moisture analyses, this present study examines the atmospheric variability on scales ranging from synoptic to intraseasonal for the period leading up to the convectively active phase of an ISO. The ISO-scale variability resembles that of the MJO active phase found in previous studies. Detailed examinations of time series show that heat and moisture fields are dominated by synoptic-scale variability. Of particular note, a moist layer extends progressively deeper in a stepwise fashion in conjunction with the passage of easterly propagating cloud systems (EPCSs) at about a 6-day period. The eventual initiation of the convectively active phase accompanied the passage of an EPCS, which led us to investigate the role of these systems in the onset of the ISO's active phase.

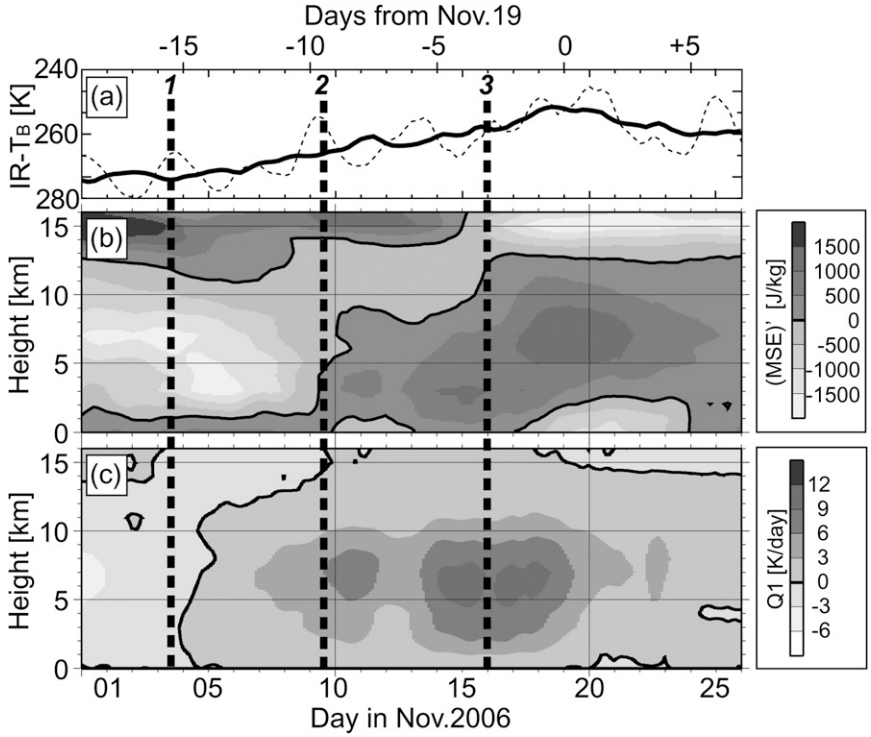

FIG. 13. Temporal variation of observed fields averaged over the MISMO triangle in Fig. 1, for (a) IR-T_B (same as in Fig. 2). (b) Time–height cross section Q_1, and (c) time–height cross section of moist static energy. A 5-day running mean is applied to (b) and (c).

This study has revealed several important aspects of the EPCSs. The EPCSs had a similar structure to that of moist Kelvin waves found in previous studies. From the analysis of radar data and Q_1, it would appear that the EPCSs contain abundant shallow precipitation and associated heating, which would project on high vertical wavenumber modes and possibly explain their slow propagation speed ($\sim$8 m s^{-1}). The analysis also showed a decreasing CIN makes the possible favorable environment for convection prior to the EPCS events. Frictional convergence from Kelvin waves could be effective at decreasing CIN.

This study focused on the heat and moisture variability and its processes, especially related to the synoptic-scale disturbances in the period prior to the onset of the ISO convectively active phase. The role of the EPCSs in this preonset is to deepen the moisture layer. A similar vertical growth of the moist layer was observed in the previous studies as the ''preconditioning'' for the MJO active phase (e.g., Lin and Johnson 1996; Johnson et al. 1999; Kemball-Cook and Weare 2001; Kikuchi and Takayabu 2004). These earlier studies emphasized the importance of the shallow convection (cumulus and congestus) as a vertical transporter of water vapor. In the present case, the abundance of shallow convection, especially before the EPCSs—which was shown in Y08 (Fig. 7 in their paper)—implies that shallow convection also directly acted to moisten the free atmosphere. The present study, however, emphasizes an alternate role for shallow convection—the driving force for the EPCSs, which in turn, transport water vapor. As a result, the shallow convection indirectly acted to moisten the troposphere. With this new role of shallow convection proposed in this study, we emphasize the importance of the shallow convection on the onset process of the ISO's convectively active phase.

Yet another important role of the EPCSs is the frictional convergence ahead of the EPCS itself. Previous studies (e.g., Maloney and Hartmann 1998; Kemball-Cook and Weare 2001; Seo and Kim 2003) have shown the existence of moisture convergence preceding the MJO active phase, with frictional convergence its primary source. Although these studies focused on the scale of ISO, the present study implies the frictional convergence also works in the synoptic scale as in individual EPCSs. The frictional convergence could also be the accumulator of the moist static energy in the lower troposphere ahead of the EPCSs.

Finally, we discuss the temporal evolution of the environment leading to the ISO convectively active phase. The deepest moisture was present in the last half of November

(see Fig. 4b). In this moisture-rich environment, the third and final EPCS of this period persisted longer and propagated farther east (Fig. 2), consisting of more developed convection (with a higher stratiform fraction; Fig. 3) and a larger Q_1, Q_2, and $-\partial(\omega' h')/\partial p$ (Fig. 5). It would appear that the increased moisture allowed for greater development and organization and, thus, a longer-lived coupled wave. Conversely, the humidity in the middle and upper troposphere increased with each EPCS passage. These results suggest that the EPCSs and environmental conditions interacted in a favorable way, which led to the ISO convectively active phase. If the present case can be viewed as the initialization of the MJO, then this concept supports the recharge–discharge mechanism for MJO initiation (e.g., Bladé and Hartmann 1993; Hu and Randall 1994). However, the effects of the EPCSs suggest that the local forcing by the convection is organized on the synoptic scale rather than stochastically.

The results of the present case study prompt additional questions that require further analyses. For example, the behavior of the convective systems within the synoptic disturbances should be investigated to reveal their detailed nature. The precise mechanism that connects the shallow convection to drive the EPCSs should be examined further. The prominence of the 6-day cycle of the EPCSs over the 3-day cycle or signal in between EPCSs is also of interest. Although the present study focused on the local processes in the Indian Ocean, factors from outside the Indian Ocean that affect the ISO-scale variability (e.g., Hendon 1988; Hsu et al. 1990; Kikuchi and Takayabu 2003) should be also examined. Because this paper presents a case study of a single ISO captured during MISMO, it is also important to understand to what degree the results presented here can be generalized to other ISO cases, including the MJO.

Recent success in reproducing the MJO with high-resolution global circulation models (e.g., Miura et al. 2007) and increasing observations with the latest satellite and buoy data [e.g., A-Train, Global Precipitation Measurement (GPM), and Research Moored Array for African–Asian–Australian Monsoon Analysis and Prediction (RAMA; McPhaden et al. 2009)] will certainly contribute to further understanding of the ISO, including the MJO onset in the Indian Ocean. On the other hand, ground-based observations are still required to reveal the detailed processes in other events. Well-designed sounding networks are especially useful for accurate analysis of the heating fields, which must be obtained if our understanding of the ISO is to be advanced. At present, detailed temporal variations in atmospheric fields can best be obtained with these ground-based sounding networks. Ground-based scanning radars are still the most useful tool to obtain the details of convective systems. Additional field campaigns over the Indian Ocean with ground-based sounding and radar networks, enhanced beyond the configuration used in MISMO, are still needed to help unravel the complex interactions between waves and convection in this region, and their relationship to MJO onset.

Acknowledgments. The authors thank Drs. H. Miura, E. Maloney, K. Yasunaga, K. Yoneyama, H. Yamada, J. Suzuki, H. H. Hendon, and an anonymous reviewer for their comments and suggestions to improve this manuscript. All participants of the MISMO project are acknowledged for their effort in obtaining the high-quality dataset. Dr. T. L'Ecuyer provided the Q_R dataset. Dr. K. Yasunaga helped a part of the analyses. The data of *Meteosat-5* is provided by EUMETSAT. Partial support for this research comes from the JEPP-HARIMAU project, and from the Joint Research Program of the Institute of Low Temperature Science, Hokkaido University. Richard Johnson and Paul Ciesielski were supported under NASA Grant NNX07AD35G.

REFERENCES

Bladé, I., and D. L. Hartmann, 1993: Tropical intraseasonal oscillations in a simple nonlinear model. *J. Atmos. Sci.,* **50,** 2922–2939.

Chen, S. S., R. A. Houze Jr., and B. E. Mapes, 1996: Multiscale variability of deep convection in relation to large-scale circulation in TOGA COARE. *J. Atmos. Sci.,* **53,** 1380–1409.

Ciesielski, P. E., R. H. Johnson, P. T. Haertel, and J. Wang, 2003: Corrected TOGA COARE sounding humidity data: Impact on diagnosed properties of convection and climate over the warm pool. *J. Climate,* **16,** 2370–2384.

Hayashi, Y.-Y., and A. Sumi, 1986: The 30-40 day oscillations simulated in an "aqua planet" model. *J. Meteor. Soc. Japan,* **64,** 451–467.

Hendon, H. H., 1988: A simple model of the 40-50 day oscillation. *J. Atmos. Sci.,* **45,** 569–584.

——, and B. Liebmann, 1991: The structure and annual variation of antisymmetric fluctuations of tropical convection and their association with Rossby-gravity waves. *J. Atmos. Sci.,* **48,** 2127–2140.

Hsu, H., B. Hoskins, and F.-F. Jin, 1990: The 1985/86 intraseasonal oscillation and the role of the extratropics. *J. Atmos. Sci.,* **47,** 2227–2240.

Hu, Q., and D. A. Randall, 1994: Low-frequency oscillations in radiative-convective systems. *J. Atmos. Sci.,* **51,** 1089–1099.

Johnson, R. H., and P. E. Ciesielski, 2000: Rainfall and radiative heating rates from TOGA COARE atmospheric budgets. *J. Atmos. Sci.,* **57,** 1497–1514.

——, T. M. Rickenbach, S. A. Rutledge, P. E. Ciesielski, and W. H. Schubert, 1999: Trimodal characteristics of tropical convection. *J. Climate,* **12,** 2397–2418.

Katsumata, M., T. Ushiyama, K. Yoneyama, and Y. Fujiyoshi, 2008a: Combined use of TRMM/PR and disdrometer data to correct reflectivity of ground-based radars. *SOLA,* **4,** 101–104, doi:10.2151/sola.2008-026.

——, and Coauthors, 2008b: Intercomparison between heat and moisture budget analyses and surface- and satellite-based observed rainfall during MISMO-IOP (in Japanese). *Proc. 2008*

Fall Meeting of Meteorological Society of Japan, Sendai, Japan, Meteorological Society of Japan, C163.

Kemball-Cook, S., and B. C. Weare, 2001: The onset of convection in the Madden–Julian oscillation. *J. Climate,* **14,** 780–793.

Kikuchi, K., and Y. N. Takayabu, 2003: Equatorial circumnavigation of moisture signal associated with the Madden–Julian oscillation (MJO) during boreal winter. *J. Meteor. Soc. Japan,* **81,** 851–869.

——, and ——, 2004: The development of organized convection associated with the MJO during TOGA COARE IOP: Trimodal characteristics. *Geophys. Res. Lett.,* **31,** L10101, doi:10.1029/2004GL019601.

Kiladis, G. N., K. H. Straub, and P. T. Haertel, 2005: Zonal and vertical structure of the Madden–Julian oscillation. *J. Atmos. Sci.,* **62,** 2790–2809.

L'Ecuyer, T. S., and G. L. Stephens, 2003: The tropical oceanic energy budget from the TRMM perspective. Part I: Algorithm and uncertainties. *J. Climate,* **16,** 1967–1985.

Lin, J., B. Mapes, M. Zhang, and M. Newman, 2004: Stratiform precipitation, vertical heating profiles, and the Madden–Julian oscillation. *J. Atmos. Sci.,* **61,** 296–309.

Lin, X., and R. H. Johnson, 1996: Heating, moistening, and rainfall over the western Pacific warm pool during TOGA COARE. *J. Atmos. Sci.,* **53,** 3367–3383.

Madden, R. A., and P. R. Julian, 1972: Description of global-scale circulation cells in the tropics with a 40-50 day period. *J. Atmos. Sci.,* **29,** 1109–1123.

Maloney, E. D., 2009: The moist static energy budget of a composite tropical intraseasonal oscillation in a climate model. *J. Climate,* **22,** 711–729.

——, and D. L. Hartmann, 1998: Frictional moisture convergence in a composite life cycle of the Madden–Julian oscillation. *J. Climate,* **11,** 2387–2403.

Mapes, B. E., and R. A. Houze Jr., 1995: Diabatic divergence profiles in western Pacific mesoscale convective systems. *J. Atmos. Sci.,* **52,** 1807–1828.

Masunaga, H., T. S. L'Ecuyer, and C. D. Kummerow, 2006: The Madden–Julian oscillation recorded in early observations from the Tropical Rainfall Measuring Mission (TRMM). *J. Atmos. Sci.,* **63,** 2777–2794.

McPhaden, M. J., and Coauthors, 2009: RAMA: The Research Moored Array for African–Asian–Australian Monsoon Analysis and Prediction. *Bull. Amer. Meteor. Soc.,* **90,** 459–480.

Miura, H., M. Satoh, T. Nasuno, A. Noda, and K. Oouchi, 2007: A Madden–Julian oscillation event realistically simulated by using a global cloud-resolving model. *Science,* **318,** 1763–1765.

Mori, K., 1995: Equatorial convection observed by the research vessel Keifu Maru during the TOGA COARE IOP, November 1992. *J. Meteor. Soc. Japan,* **73,** 491–508.

Nakazawa, T., 1988: Tropical super clusters within intraseasonal variations over the western Pacific. *J. Meteor. Soc. Japan,* **66,** 823–836.

Nicholls, M. E., R. A. Pielke, and W. R. Cotton, 1991: Thermally forced gravity waves in an atmosphere at rest. *J. Atmos. Sci.,* **48,** 1869–1884.

Nuss, W. A., and D. W. Titley, 1994: Use of multiquadric interpolation for meterological objective analysis. *Mon. Wea. Rev.,* **122,** 1611–1631.

Ohuchi, K., and M. Yamasaki, 1997: Kelvin wave-CISK controlled by surface friction: A possible mechanism of super cloud cluster. Part I: Linear theory. *J. Meteor. Soc. Japan,* **75,** 497–511.

Seo, K.-H., and K.-Y. Kim, 2003: Propagation and initiation mechanisms of the Madden–Julian oscillation. *J. Geophys. Res.,* **108,** 4384, doi:10.1029/2002JD002876.

Straub, K. H., and G. N. Kiladis, 2003a: Interactions between the boreal summer intraseasonal oscillation and higher-frequency tropical wave activity. *Mon. Wea. Rev.,* **131,** 945–960.

——, and ——, 2003b: The observed structure of convectively coupled Kelvin waves: Comparison with simple models of coupled wave instability. *J. Atmos. Sci.,* **60,** 1655–1668.

Takahashi, S., F. Kondo, O. Tsukamoto, Y. Ito, S. Hirayama, and H. Ishida, 2005: On-board automated eddy flux measurement system over open ocean. *SOLA,* **1,** 37–40, doi:10.2151/sola.2005-011.

Takayabu, Y. N., 1994: Large-scale cloud disturbances associated with equatorial waves. Part I: Spectral features of the cloud disturbances. *J. Meteor. Soc. Japan,* **72,** 433–449.

Tulich, S. N., and B. E. Mapes, 2008: Multiscale convective wave disturbances in the tropics: Insights from a two-dimensional cloud-resolving model. *J. Atmos. Sci.,* **65,** 140–155.

——, D. A. Randall, and B. E. Mapes, 2007: Vertical-mode and cloud decomposition of large-scale convectively coupled gravity waves in a two-dimensional cloud-resolving model. *J. Atmos. Sci.,* **64,** 1210–1229.

Wang, B., and H. Rui, 1990: Synoptic climatology of transient tropical intraseasonal convection anomalies: 1975–1985. *Meteor. Atmos. Phys.,* **44,** 43–61.

Webster, P. J., and R. Lukas, 1992: TOGA COARE: The coupled ocean-atmosphere response experiment. *Bull. Amer. Meteor. Soc.,* **73,** 1377–1416.

Wheeler, M., and G. N. Kiladis, 1999: Convectively coupled equatorial waves: Analysis of clouds and temperature in the wavenumber-frequency domain. *J. Atmos. Sci.,* **56,** 374–399.

——, and K. M. Weickmann, 2001: Real-time monitoring and prediction of modes of coherent synoptic to intraseasonal tropical variability. *Mon. Wea. Rev.,* **129,** 2677–2694.

Wu, Z., 2003: A shallow CISK, deep equilibrium mechanism for the interaction between large-scale convection and large-scale circulations in the tropics. *J. Atmos. Sci.,* **60,** 377–392.

Yanai, M., S. Esbensen, and J.-H. Chu, 1973: Determination of bulk properties of tropical cloud clusters from large-scale heat and moisture budgets. *J. Atmos. Sci.,* **30,** 611–627.

Yoneyama, K., M. Fujita, N. Sato, M. Fujiwara, Y. Inai, and F. Hasebe, 2008a: Correction for radiation dry bias found in RS92 radiosonde data during the MISMO field experiment. *SOLA,* **4,** 13–16.

——, and Coauthors, 2008b: MISMO field experiment in the equatorial Indian Ocean. *Bull. Amer. Meteor. Soc.,* **89,** 1889–1903.

Yu, J.-Y., and J. D. Neelin, 1994: Modes of tropical variability under convective adjustment and the Madden–Julian oscillation. Part II: Numerical results. *J. Atmos. Sci.,* **51,** 1895.

Yu, L., X. Jin, and R. A. Weller, 2008: Multidecade global flux datasets from the objectively analyzed air-sea fluxes (OAFlux) project: Latent and sensible heat fluxes, ocean evaporation, and related surface meteorological variables. OAFlux Project Tech. Rep., Woods Hole Oceanographic Institution, 64 pp.

Yuter, S. E., R. A. Houze Jr., E. A. Smith, T. T. Wilheit, and E. Zipser, 2005: Physical characterization of tropical oceanic convection observed in KWAJEX. *J. Appl. Meteor.,* **44,** 385–415.

Zhang, C., 2005: Madden–Julian oscillation. *Rev. Geophys.,* **43,** RG2003, doi:10.1029/2004RG000158.